The influence of temperature on deformation-induced martensitic transformation in 301 stainless steel

Yadunandan B. Das[1, 2*], Alexander N. Forsey[1], Joe Kelleher[3], Saurabh Kabra[3], Michael E. Fitzpatrick[4], Thomas H. Simm[5], Salih Gungor[1], Richard J. Moat[1**]

1. *Materials Engineering, The Open University, Walton Hall, Milton Keynes MK7 6AA, UK*
2. *Department of Material Science and Engineering, KTH Royal Institute of Technology, Stockholm SE-10044, Sweden*
3. *ISIS facility, Rutherford Appleton Laboratory, Didcot OX11 0QX, Oxfordshire, UK*
4. *Faculty of Engineering and Computing, Coventry University, Priory Street, Coventry CV1 5FB, UK*
5. *College of Engineering, Swansea University, Bay Campus, Swansea SA1 8EN, UK*

[*]*yadunandan.das@gmail.com*, [**]*richard.moat@open.ac.uk*

Abstract

Deformation-induced martensitic transformations are increasingly being used to create desirable mechanical properties in steels. Here, the kinetics of the deformation-induced martensitic transformation is investigated at 300 K, 263 K, 223 K, 173 K and 100 K using in situ neutron diffraction during tensile loading. The results from these experiments show a distinct change in the transformation behaviour between 300 K and the tests conducted at 263 K and below, causing a difference in martensite structure. The difference in transformation kinetics is correlated to the suppression of slip at low temperatures, as evidenced using diffraction peak intensity analysis for different grain families and corroborated using transmission electron microscopy. A direct correlation between the deformation-induced martensite fraction and work-hardening rate is shown.

Keywords: Neutron Diffraction, solid-state transformation, martensite, TRIP steel, work hardening

1 Introduction

Solid-state transformations, such as martensitic transformations, are now commonly being used to improve the mechanical properties of structural steels [1–3]. Furthermore, because strengthening is a result of phase transformation, this is achieved without any increase in the overall mass, and may lead to greater fuel efficiency when applied to applications such as the automotive industry [4–7]. Therefore martensite, which is traditionally considered to have poor mechanical properties due to problems

associated with reduced toughness and formability, may be exploited to improve the mechanical properties of steels [8]. It is now known that steels strengthened by deformation-induced martensite exhibit high yield strength whilst demonstrating exceptional ductility [9]. Over recent decades martensitic transformations have been thoroughly studied [5,10–13], however, with improvements in measurement technology, characterisation tools and modelling capabilities, they are still of great interest to the research community [4,14–18].

Usually, austenitic stainless steels are stable at room temperature and only transform to martensite when they are cooled to temperatures below their martensite start temperature (M_s). However, when the driving force is insufficient for spontaneous transformation to occur, the application of an external stress can supply sufficient mechanical energy for a deformation-induced transformation to occur [19–22]. Zackay *et al*. [8] first introduced the concept of transformation-induced plasticity (TRIP) steels, which are a class of steels that exploit the deformation-induced martensitic transformations. The microstructure of most TRIP steels comprise of a minor fraction of metastable austenite (γ) within a matrix of ferrite and/or bainite. Upon loading, as a consequence of additional strain energy the retained austenite is transformed, to form deformation-induced martensite [23]. Moat *et al*. [4] investigated one such commercially interesting steel that showed the TRIP phenomenon, where localised areas of retained austenite phase transformed into deformation-induced martensite on application of external load. Jimenez-Melero *et al*. [24] and Blonde *et al*. [25] investigated the stability of individual austenite grains in a low-alloy TRIP steel as it was cooled down to form martensite using synchrotron X-ray diffraction. Collectively [24,25], they showed how the stability of individual grains varied, with some grains transforming completely, some grains partially transforming, while some very stable grains did not transform at all. Further, Jimenez-Melero *et al*. [24] and Blonde *et al*. [25] showed that grains with the lowest carbon content and the highest grain volume had the least stability and transformed at higher temperatures during the cooling process. Blonde *et al*. [25] considered diffraction peaks parallel to the loading direction, they showed at cryogenic test temperatures (153 K) that an increase in plastic deformation, caused an enhanced tendency for a reduction in the intensity of the {220}, {200} and {311} austenite reflections compared to the {111} and {222}. A pronounced tendency for martensite to form on grains oriented with the {200} parallel to the loading direction at the lower temperatures was also illustrated. Unfortunately, the microstructure and phase composition of alloys investigated by Blonde *et al*. [25] and Moat *et al*. [4] is believed to be too complex, owing to the presence of ferrite, martensite and bainite simultaneously, to enable the isolation of individual transformation events, determine strains within individual metastable austenite grains, or predict the crystallography of TRIP martensite. Although, the such studies cannot distinguish the bcc ferrite, bainite and martensite, the one step transformation has been successfully monitored *in situ* during both cooling

[24,26,27] and mechanical loading [28], where the main microstructural parameters controlling the austenite stability were determined.

For deformation-induced martensitic transformation to occur, the austenite parent lattice is plastically deformed, creating potential nucleation sites on which transformation can occur. Olson and Cohen [29,30] proposed that this deformation within the austenite parent lattice is localised to areas of planar faults, such as shear band intersections, so that further deformation triggers the formation of martensite. Some of the more recent work by Talonen [31], using scanning electron microscopy and electron channelling contrast imaging, confirmed this observation. Hedström *et al.* [32] conducted various synchrotron X-ray diffraction studies to look at the effect of deformation-induced transformation and found an autocatalytic sequence of transformations, which were evidenced as bursts of deformation-induced α′ on loading. They proposed that residual stress fields around such transformation sites lead to localised hardening, provide resistance to necking, and ultimately improve the mechanical properties of the metastable austenite [32,33], supporting the theory proposed by Zackay *et al*. [8]. They also observed that both α′-martensite and ε-martensite formed on deformation of a 301 metastable austenitic stainless steel. Hedström *et al.* [34] showed the structural evolution of deformation-induced α′ could be quantified three-dimensionally in individual austenite grains using synchrotron X-rays. They showed that large differences in lattice strain might be observed in grains having nearly identical crystallographic orientation, which may further be influenced by the local grain environment. More recently, Lee *et al*. [35,36] studied the correlation between the stacking fault energy and the deformation structures of austenitic steels. They found that deformation bands/planar defects had distinct structure and that α′ and ε-martensite phases occurred at the intersection of these deformation regions.

The authors have previously studied the deformation-induced martensitic transformation in type 301-austenitic stainless steel using high-resolution digital image correlation (HR-DIC) and EBSD, and compared the predicted transformations with experimental observations [17]. The same material is used for the investigations in this article. It is well-known that on deforming this material at room temperature it readily transforms to martensite [1,31,33,37]. Furthermore, on account of having an almost fully austenitic initial microstructure, this material is ideal to isolate and study the newly forming martensite plates, while avoiding the complications reported in reference [25]. In this study, experiments were conducted at 300 K, 263 K, 223 K, 173 K and 100 K to study the difference in the mode of transformation, and subsequent effect on mechanical behaviour of the alloy. The deformation-induced martensitic transformations were studied here by *in situ* neutron diffraction at the ENGIN-X diffractometer at the UK's ISIS facility [38,39], using a newly-commissioned cryogenic chamber capable of temperatures in the range 6 K to 300 K [40].

2 Experimental details

The ENGIN-X beamline [39] was used to quantify the phase fraction evolution during tensile loading at various temperatures between 300 K and 100 K. Microstructural characterisation of the deformation-induced martensite was then performed using a JEOL JEM 2100 transmission electron microscope (TEM).

2.1 Material

A type 301 austenitic stainless steel, having nominally fully austenitic structure (FCC), was used for this work. The complications of analysis that may arise owing to other BCC type phases such as ferrite and bainite, which are often difficult to differentiate from martensite using neutron diffraction, are mitigated by using a purely austenitic starting structure. The material was received in a fully annealed condition and its chemical composition is as given in Table 1.

Table 1. The chemical composition of a 301 austenitic stainless steel in weight %.

Fe	C	Si	Mn	P	S	Cr	Ni	Cu	Mo
Bal.	0.001	0.48	1.057	0.043	0.001	16.98	7.12	0.381	0.311

Flat test specimens with dog-bone-shaped cross section, were electro-discharge machined from a 1.6 mm thick plate. The sample dimensions were similar to the sample dimensions of a standard ASTM E8M[41] sub-size specimen (width 6 mm and gauge length 25 mm), but with shorter grip sections as shown in Figure 1. Specially designed aluminium grips were manufactured because the test temperatures used were below the ductile/brittle transition temperature of standard steel grips and aluminium has a good thermal conductivity to minimise the time needed to reach a stable temperature.

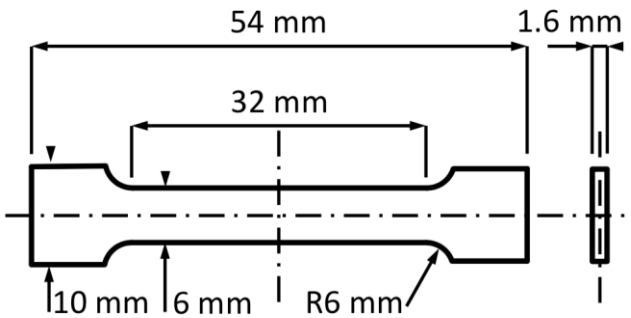

Figure 1: Sample design and dimensions

2.2 ENGIN-X instrument

Figure 2 (a) schematically shows the ENGIN-X diffractometer; which has two fixed-angle detector banks, each centred on a Bragg angle 2θ of ±90°, at approximately 1.5 m from the instrument gauge volume, positioned behind the radial collimators [39]. This allows for the measurement of diffraction data from two orthogonal directions simultaneously. The detectors cover an angular range of 76 - 104° in 2θ on either side of the incident beam [42]. Furthermore, as a time-of-flight diffractometer, the entire diffraction pattern (many {hkl} planes) is measured in a single exposure during the *in situ* deformation process. Although ENGIN-X's main design purpose is to make engineering strain measurements by the accurate measurement and mapping of lattice strain at precise locations [39], it has been successfully used for investigating phase transformations by Oliver *et al.* [43] and more recently Moat *et al.* [4].

2.3 Neutron diffraction measurements

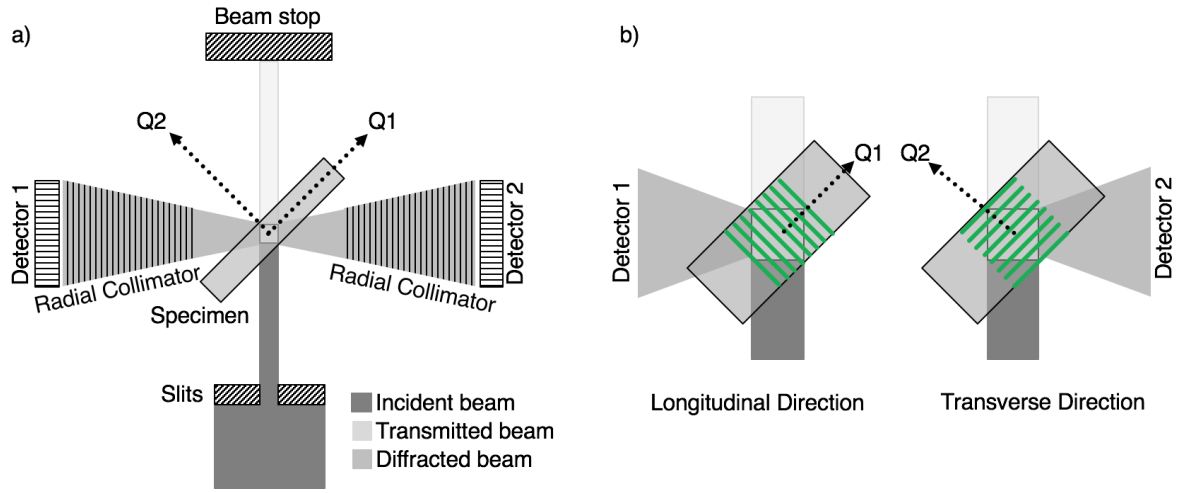

Figure 2: (a) Schematic of ENGIN-X. (b) Diffracted beams measured in Detector 1 (longitudinal direction) and in Detector 2 (transverse direction) (not to scale)

As shown in Figure 2 (a), the samples were aligned at angles of ±45° to the incident beam. Because ENGIN-X is set up with each detector at 90° to the incident beam, positioning the sample at 45° ensures that diffraction is collected from grains with lattice planes satisfying the Bragg criterion aligned along the longitudinal ($Q_{//}$) and transverse directions ($Q_{\perp}$) (±14° as a consequence of the angular spread of the collimators). When set this way, measurements in Detector 1 are from lattice planes perpendicular to the longitudinal ($Q_{//}$) direction of the sample and the measurements in Detector 2 are from lattice planes perpendicular to the transverse ($Q_{\perp}$) direction (see Figure 2 (b)). The positioner table was motorized and programmed for movements in x, y, z and ω directions. It can hold samples that weigh up to 800 Kg, making positioning a servo-hydraulic tensile rig to the sub-millimetre precision required possible [44].

In order to maintain reasonable resolution with respect to the change in martensite fraction in both the elastic and plastic regimes, the load rig control method was changed during the test. While the material was in the elastic regime, the tests were performed in load control and after the material's yield strength had been exceeded the tests were changed to position control. In the plastic region, the work hardening rate is initially low and a small increase in stress can result in a very large increase in strain. Therefore, a change in control mode is needed to have sufficient strain increment resolution. During the load control stage, each sample was loaded from 50 MPa to 400 MPa in 50 MPa load increments. After the sample was loaded to 400 MPa, it was strained in 0.3 mm increments, equivalent to strain increments of ~ 1.2 %. For each measurement point, neutrons were collected for 20 micro amp hours of proton current, which equates to a count time of approximately 15 minutes.

A total of five *in situ* tests were performed, each at a different temperature. A custom-built, liquid-helium cryogenic chamber [40] available at the ENGIN-X facility was fitted to the Instron tensile frame. Copper couplings were connected from the cryostat to the load frame and temperature was monitored using K-type thermocouples attached to the sample. The samples were "over" cooled and the desired temperature was controlled through heaters placed in the sample grips. Temperatures of 300 K, 263 K, 223 K, 173 K and 100 K were set while the sample load was set to 0 MPa and maintained in load control to ensure deformation was not induced during cooling. Tensile testing only commenced once the temperature read on the thermocouple was stable.

2.3.1 Neutron data treatment

Traditional peak position analysis for stain and load partitioning determination, such as the work by Harjo *et al.* [45] and Moat *et al.* [4], is deemed not appropriate in this case. This is because the sample and instrument design render the gauge volume of the instrument not fully filled. Here even a slight movement in the test specimen within the instrument gauge volume will dramatically change the centre of gravity of the sample gauge volume [46], resulting in large shifts in the peak position not attributable to strain. Furthermore, during transformation events, the disappearance of austenite and appearance of martensite peaks do not necessarily occur evenly across the diffraction peak. In fact, due to variations in stress and/or the carbon content occurring across the *d* spacing range of a diffraction peak, it is completely expected that austenite grains contributing to a particular portion of the diffraction peak will disappear or appear preferentially, because they will represent extremes in the carbon content or stress. This results in a statistical shift in peak centre in the absence strain. For these reasons it was decided to omit analysis of peak strain and load partitioning and concentrate on the peak intensity analysis to develop greater understanding of the differences in transformation at various temperatures.

Austenite and martensite phase volume fractions were calculated from individual diffraction peak intensities using Equation 1 outlined in ASTM standard E 957-03 [47], which is the standard expression used for retained austenite volume fraction determination in steels.

$$V_\gamma = [\frac{1}{q}\sum_{j=1}^{q}\frac{I_{\gamma j}}{R_{\gamma j}} / \{\left(\frac{1}{p}\sum_{i=1}^{p}\frac{I_{\alpha j}}{R_{\alpha j}}\right) + \left(\frac{1}{q}\sum_{j=1}^{q}\frac{I_{\gamma j}}{R_{\gamma j}}\right)\}] \qquad \textit{Equation 1}$$

Where I_γ and I_α are the integrated intensities of the austenite and martensite reflections respectively; and R_γ and R_α are the Rietveld number for the respective phases (*i.e.,* the theoretical relative intensity of that reflection). However, this equation does not take into account of the hexagonal epsilon martensite phase, which was also measured here and therefore the equation was modified as follows:

$$V_\gamma = [\frac{1}{q}\sum_{j=1}^{q}\frac{I_{\gamma j}}{R_{\gamma j}} / \{\left(\frac{1}{p}\sum_{i=1}^{p}\frac{I_{\alpha j}}{R_{\alpha j}}\right) + \left(\frac{1}{q}\sum_{j=1}^{q}\frac{I_{\gamma j}}{R_{\gamma j}}\right) + \left(\frac{1}{r}\sum_{j=1}^{r}\frac{I_{\varepsilon j}}{R_{\varepsilon j}}\right)\}] \qquad \textit{Equation 2}$$

Where I_ε and R_ε are the integrated intensity and Rietveld number of the epsilon martensite reflection respectively. A similar approach was used by Hedström *et al*. [32] and De *et al*.[48,49] for volume fraction measurements using high-energy X-ray diffraction and laboratory X-ray diffraction respectively. Thus, by analysing the diffraction peak intensities of the several {*hkl*} peaks, volume fraction calculations using Equation 1 and Equation 2 become less sensitive to texture than when comparing a single pair of diffraction peak intensities.

2.4 TEM sample preparation and procedure

The deformation-induced martensite structures were observed by TEM to characterise their structure and morphology. Specimens for TEM observations were prepared by grinding and polishing regions of the deformed tensile test pieces from within the gauge volume, to thicknesses less than 100 µm. From these sheets, 3-mm-diameter discs were punched out and further thinned using jet electro-polishing. The electrolyte used was 5% perchloric acid in methanol, the voltage was set to 20 V and the temperature was kept below –50°C throughout the thinning process. TEM observations were made using a JEOL JEM 2100 microscope operated at 200 kV, and images were acquired in bright field and STEM modes.

3 Results

3.1 Mechanical properties

Figure 3 shows the stress-strain curves for tensile loading at all five measurement temperatures. At 300 K, after yielding, an approximately constant work hardening rate is observed. For the cryogenic temperature experiments, upon yielding, stress remains almost constant until between 6-7% strain

whereupon a sharp increase in work-hardening rate is observed. A similar observation was reported by Hecker *et al.*[22] and Spencer *et al.* [50]. Spencer *et al.* [50] showed that the much stiffer deformation-induced martensite phase acted as an elastic reinforcing phase and carried much higher stresses before deformation compared to the parent austenite.

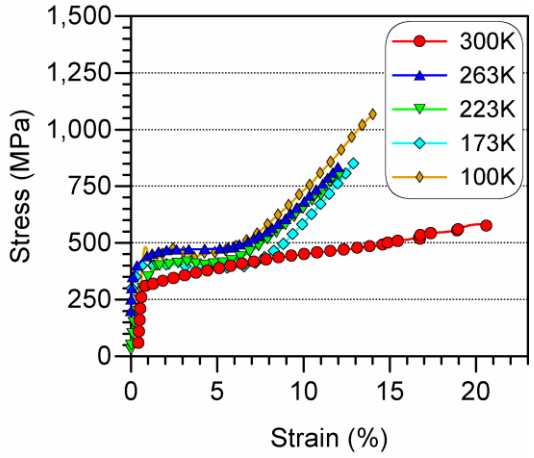

Figure 3: Stress-strain curve for tensile loading at 300 K, 263 K, 223 K, 173 K and 100 K

3.2 Neutron Diffraction

Phase fractions of individual phases were calculated, using Equation 2, for all five temperatures. Phase fraction as a function of applied strain are shown in Figure 4. At 300 K, there is a constant increase in α′ and ε martensite beyond ~2% applied strain, accompanied by a drop in austenite volume fraction. In all tests conducted at temperatures of 263 K and below, at strains slightly below 1%, the volume fraction of ε-martensite phase increases. This is followed by an increase in volume fractions of the α′-martensite phase at approximately 1.5% strain. At strain values greater than ~6%, the volume fraction of α′-martensite increases more rapidly, whereas, the volume fractions of both the austenite and ε-martensite phases decrease.

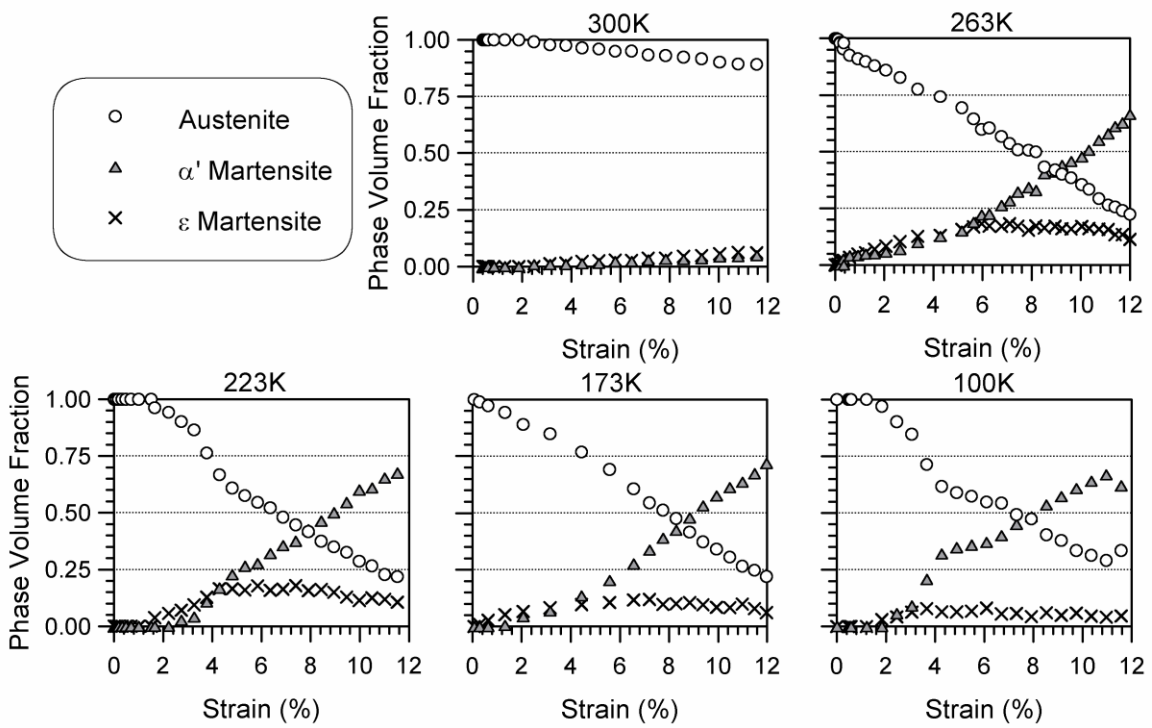

Figure 4: Volume fractions of γ- austenite, α′- martensite and ε- martensite phases at 300 K, 263 K, 223 K, 173 K and 100 K with respect to strain.

These results can be divided into two distinct transformation behaviours, with the room temperature transformation differing from all the lower temperature experiments. Figure 5 and Figure 6 show the phase fraction evolution for each test with respect to applied strain and applied stress respectively. Figure 5 further highlights the two distinct transformation behaviours: the test conducted at 300 K shows a constant rate of transformation of both α′- and ε-martensite and the corresponding reduction in austenite fraction; whilst for all four low temperature tests, initial transformation is to ε-martensite shortly followed by α′-martensite. At between 3% and 4% applied strain, the transformation rate to α′-martensite increases significantly, while at approximately 6% applied strain the ε-martensite fraction is seen to start reducing.

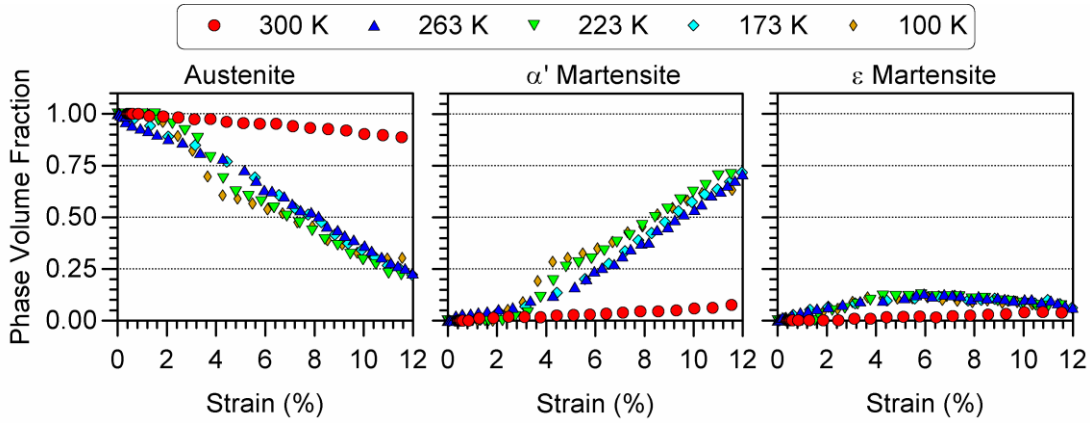

Figure 5: The change in γ, α' and ε volume fraction with applied strain, at the different measurement temperatures.

Figure 6 shows the data from the same experiments as in Figure 5, however in this figure, plots with respect to the applied stress. At 300 K, the sample was strained to over 20% strain, but only reached a maximum stress of ~575 MPa (Figure 6), owing to the absence of any significant work-hardening. The volume fraction of γ decreased at stresses above 320 MPa, with corresponding increase in the volume fraction of α'-martensite. The volume fraction of ε-martensite increased at stresses above ~350 MPa, *i.e.* α' phase nucleated before the ε martensite phase. For the low-temperature experiments, γ began transforming to ε at slightly lower stress than for α', with transformation occurring in all samples at 2-4% strain increments after yielding occurred. This indicated that elastic stress alone was not sufficient to cause observable transformation in the bulk samples. The volume fraction of the ε phase peaked at around 480 MPa for the low temperature measurements, and then decreased with further increases in applied stress.

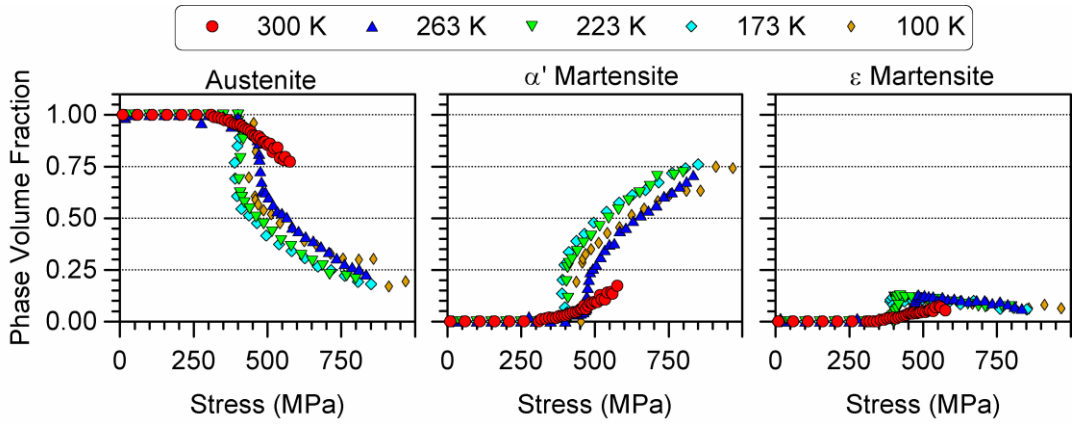

Figure 6. The change in γ, α' and ε phase intensity with the macroscopic stress, at the different measurement temperatures.

3.3 TEM

Figure 7 shows TEM photomicrographs of deformation-induced martensite. Lenticular martensite plates were observed for specimens deformed at room temperature, whereas lath martensite plates, with the presence of internal dislocations, were observed for the lower temperature experiments. From the photomicrographs, it appears that the lenticular martensite plates are comprised of a twinned substructure within them. From previous experimental works it is known that the extent of $\gamma \rightarrow \varepsilon$ or $\gamma \rightarrow \alpha'$ transformation depends on the strain, prior austenite grain size and temperature of deformation [13,49]. In the past, researchers believed that ε - martensite was a prerequisite to the formation of α'- martensite [51]. However, now there is evidence that both forms of martensite may be formed independently during the deformation of the alloy [52]. The martensite embryos result from the formation of stacking faults during the cooling or the deformation, *i.e.*, they are dislocation pile ups [53,54], or shear band intersections [31].

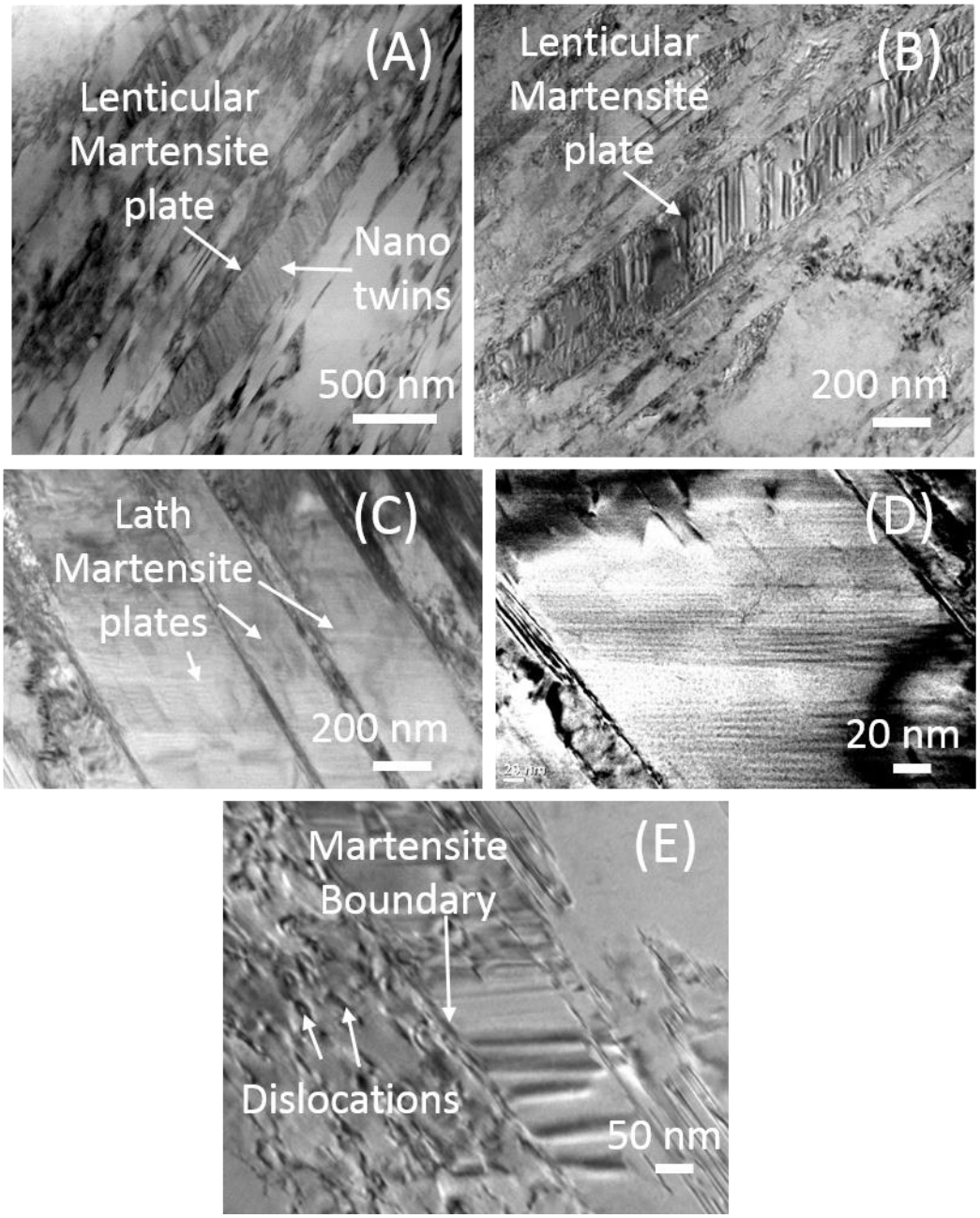

Figure 7: Characteristic TEM photomicrographs of deformation-induced martensite. (A) STEM photomicrograph and (B) bright field TEM photomicrograph of the same lenticular martensite plate with internal nano-sized twins formed due to deformation at 300 K. (C) Bright field TEM photomicrograph of lath martensite and (D) high-resolution photomicrograph of the same region formed due to deformation at 100 K. (E) Martensite plate providing a barrier for dislocation motion at 20% strain due to deformation at 300 K.

4 Discussion

The results show that tensile deformation at 300 K, 263 K, 223 K, 173 K and 100 K all result in transformation to martensite, however significantly different transformation kinetics are observed between the test conducted at 300K and the lower temperature tests. This is in line with work presented by Moat *et al.*[4], which also shows similar transformation behaviour in at –50°C (223 K) and –100°C (173 K), but a marked reduction in transformation rate at room temperature. TEM

interrogation also reveals a difference in structure between those samples deformed at 300 K and 100 K. This result indicates that a different transformation mechanism may be at work at different temperatures.

At 300 K, the first transformation product is detected after ~2% strain. This means that significant plastic deformation has occurred before the first transformation product has formed, indicating that the martensite forming is strain-induced rather than stress-assisted. In this case, the two transformation phases, ε and α', appear for the first time at the same strain increment. TEM interrogation shows a twinned, lenticular martensite forming at this temperature.

At low temperatures, the first finding to note is that prior to deformation, even after cooling to 100 K, there was no indication of martensite formation. Therefore, it is reasonable to assume that nucleation of martensite is not thermodynamically possible without the introduction of an external driving force. For all low-temperature tests, the ε phase was detected at lower strains than the α' phase. Figure 6 shows that both phases are only detected after the yield point is exceeded, which is at higher stress than for 300 K, owing to the increase in yield strength with reduction in temperature (see Figure 3). The transformation sequence of ε-martensite before α'-martensite is in keeping with that reported in literature [29,31,36,50,55]. TEM investigation of the low-temperature martensite shows a lath type structure, different to that found at 300 K.

Previous work by the authors shows that the transformation of martensite at 300 K is nucleated on {111} slip planes, confirming slip is key in nucleating martensite at this temperature [17]. That work also shows that, due to the heterogeneous nature of plasticity, some grains transform significantly, while others transform considerably less: the limitation of the work is the surface nature of microscopy [17]. In the results presented here, diffracted neutrons are collected from the entire sample volume, meaning a much greater number of grains are interrogated. The results discussed so far focus on the quantification of the volume fraction of transformation as a whole and have done so by averaging as much of the collected diffraction data as possible. Although it is not possible to quantify the transformation of individual grains, by investigating the individual diffraction peak intensities the transformation kinetics of discrete subsections of grains, often termed grain families, can be quantified. These discrete subsets of material are described by the grains fulfilling the Bragg criterion for a detector of a specific orientation *i.e.*, the longitudinal $\{200\}_\gamma$ grain family are those grains which are contributing to the {200} diffraction peak in detector 1 (see Figure 2 (b)) and therefore the normal of the {200} lattice planes is parallel to the loading direction.

Investigating the intensities of individual grain families is useful here because each subset of grains has a different average Schmid factor. The Schmid factor has been shown to be a useful quantity in

determining the active slip systems in a grain in this alloy [17], with the slip system with the highest Schmid factors being more likely to be active. And it has also been shown that in this alloy there was a correlation between increases in the Schmid factor and increases in the amount of plastic deformation, as measured by peak profiles and orientation spread [56], in different grains. The MTEX matlab toolbox[57] has been used to calculate the average Schmid factor for grains that would theoretically diffract into each of the detector banks. This is done by simulating 10,000 randomly orientated grains and determining if the plane of interest lies within ± 14° of the Bragg criterion (approximately comparable to the coverage of the ENGIN-X detector banks). Table 2 lists the calculated Schmid factors for the $\{111\}_\gamma$, $\{200\}_\gamma$ and $\{220\}_\gamma$ reflections for each of the detector banks.

Table 2: Schmid factor calculated for 3 grain families in the longitudinal and transverse direction (bold denoting the high value for its respective reflection)

Detector	Average Schmid Factor for grains fitting Bragg criterion		
	{111}	{200}	{220}
Longitudinal (Detector Bank 1)	0.3692	0.4556	**0.4594**
Transverse (Detector Bank 2)	**0.4537**	**0.4711**	0.4344

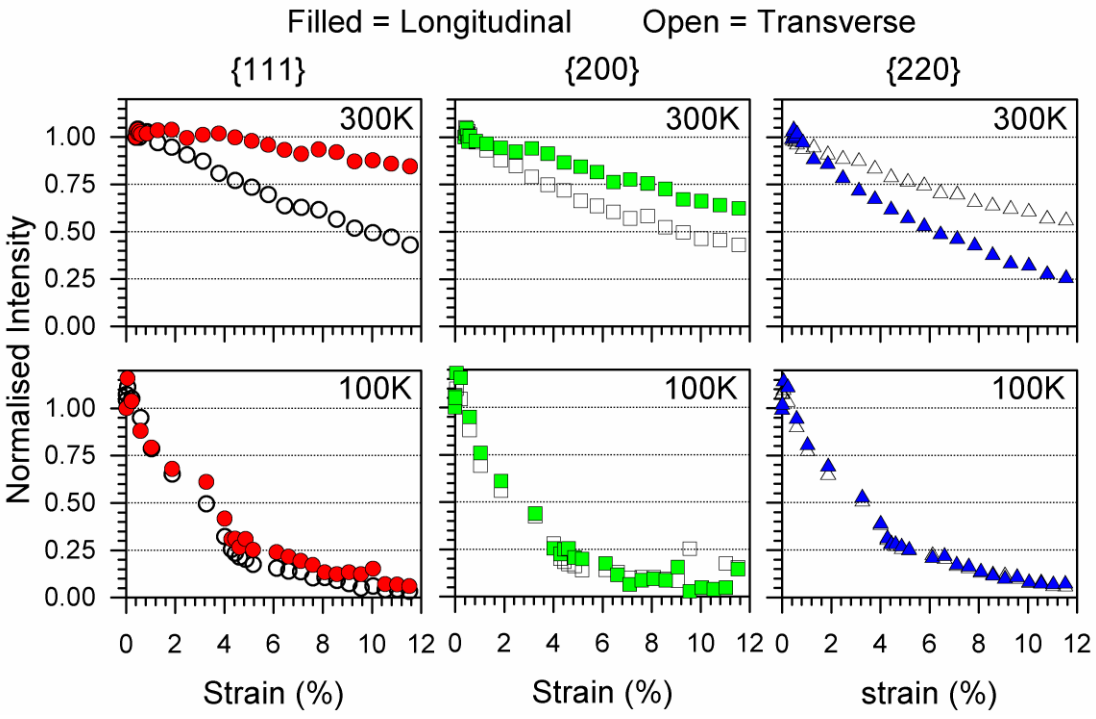

Figure 8. Normalised austenite peak intensities at 300 K and 100 K for {111}, {200} and {220} austenite reflections in the transverse and longitudinal directions.

The austenite peak intensities, normalised by the initial intensities for the measurement made at 300 K, and for 100 K, are shown in Figure 8. Because of the similarity in results for all the tests conducted

below 300 K, only 300 K and 100 K are plotted to ease interpretation and discussion. For the test conducted at 300 K, the $\{111\}_\gamma$ and $\{200\}_\gamma$ peaks reduce in intensity at the highest rate in the transverse direction, while the $\{220\}_\gamma$ peak intensity reduced more rapidly in the longitudinal direction. When compared to the calculations in Table 2, this indicates that grains which are transforming most readily into martensite are also those grains which, on average, are likely to have undergone significant amounts of plastic deformation. For 100 K, also in Figure 8, all three reflections show the same response in both directions, indicating that the likelihood of plastic deformation of the austenite is less critical in the formation of martensite at 100 K than at 300 K.

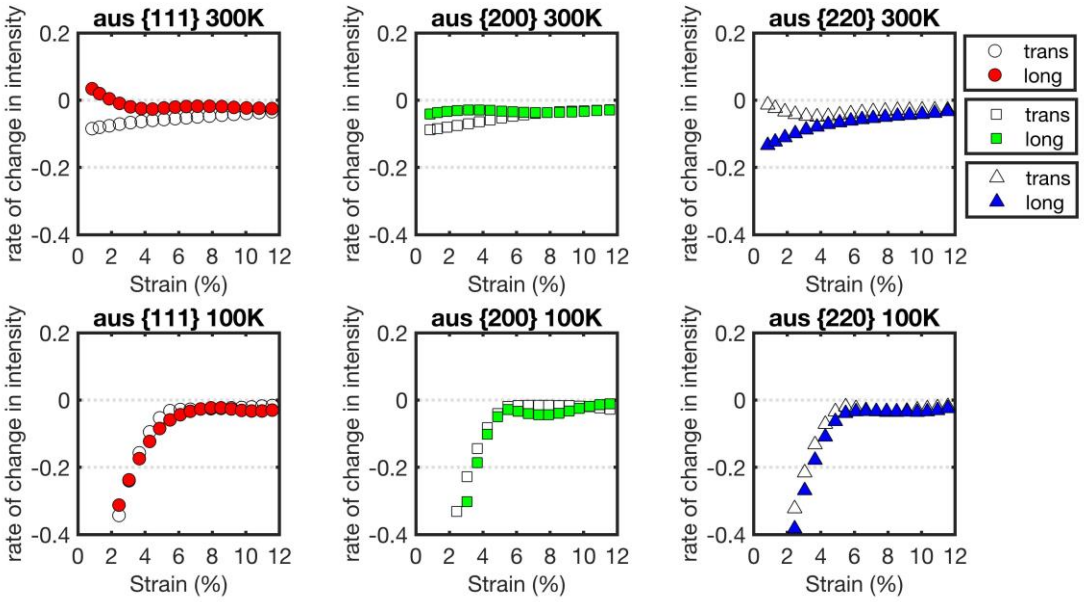

Figure 9: rate of change in austenite diffraction peak intensity for {111}, {200} and {220} in the longitudinal and transverse direction at 300K and 100K

Intergranular strain evolution and load partitioning amongst constituent phases during deformation of the alloy have not been presented in this manuscript. The reason for not including the intergranular strains was that the sample did not fill the entire gauge volume. Consequently, any movement of the sample during deformation would lead to pseudo strain measurements, compromising any conclusions made. Further, the strain free lattice parameters for the deformation induced α′ is unknown, because the martensite forms in a stressed state and the assumption that it is strain free is not valid. This fact is often overlooked in data available in literature [45]. However, the peak intensities in Figure 8 have been differentiated to show the rate of change in diffraction peak intensity, and are shown in Figure 9. The same trend is observed, where grain families with the highest Schmid factor have the highest rate of change, at least up to 7% strain, at 300 K; while at 100 K, little difference is observed between the two directions. For the test conducted at 100 K, an initial rapid decrease is observed and after ~6% strain, the rate drops to one similar to that observed for the 300 K test. This

finding can be explained in terms of accommodation of strain energy. At room temperature, slip is more energetically favourable to accommodate strain energy than the formation of transformation product with an associated transformation strain. Then, once sufficient nucleation sites have formed, this difference becomes less and less pronounced. At lower temperatures (*e.g.* 100 K), due to the suppression of slip, this is not the case and transformation strain is the dominant mechanism to accommodate strain energy. For all experimental conditions, nucleation sites are formed due to slip; these nucleation sites become more energetically favourable with decrease in temperature. This is because with decrease in experimental temperature, the thermodynamic driving force for transformation increases, *i.e.*, it is energetically favourable[20].

The significance in terms of the difference in transformation behaviours is the subsequent influence on mechanical properties. From Figure 7 (E), it appears that as deformation progresses, the newly formed deformation-induced martensite plates may act as a barrier for dislocation motion. For the propagation of dislocations across this deformation-induced martensite barrier, greater energy will be required. This phenomenon leads to localised strain hardening, which effectively provides a localised resistance to dislocation motion and the onset of necking. Furthermore, this strengthening mechanism leads to enhancement in the work hardening and ductility of the material.

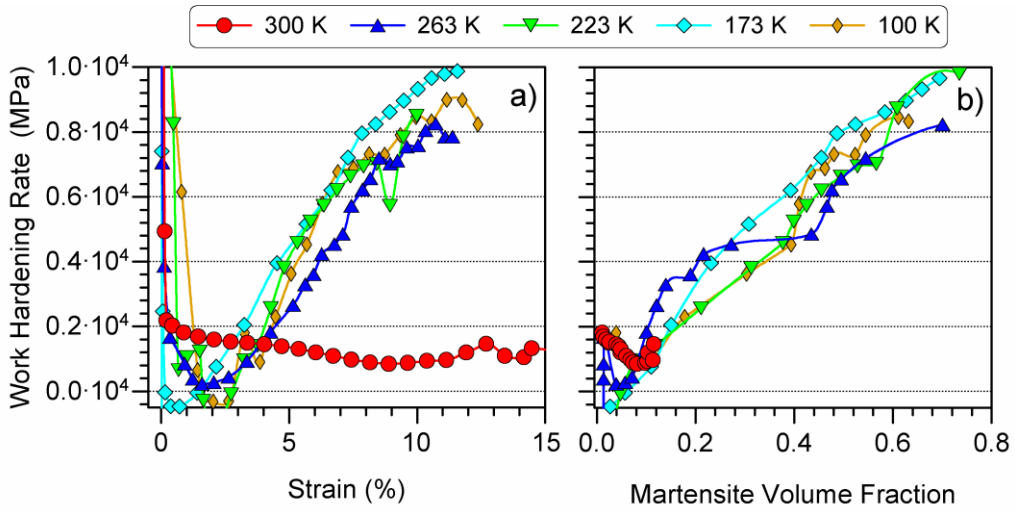

Figure 10. Slope of the stress-strain curves – giving the work hardening rate – plotted with respect to the applied macroscopic True Strain and Stress.

From a macroscopic viewpoint, insights into the transformation-induced strain hardening may be obtained by differentiating the stress-strain curves from Figure 3, and results are shown in Figure 10 (a). In Figure 10 (a), the difference in work hardening behaviour between the test conducted at 300 K and the low temperature tests is clear. Figure 10 (b) shows the work hardening rate vs the fraction of martensite formed. From this it is clear that a trend between the fraction of martensite and the work hardening rate exists. Spencer *et al*. [50], Hedström *et al*. [58] and Harjo *et al*. [45] showed that the load in

the α′ phase was almost twice that in the γ phase. However, at both the low and ambient temperatures, with increase in loading, strain hardening mechanisms and phase transformations become difficult to deconvolute, owing to the development of a composite microstructure and load transfer within it [5,7,30,51,55,59–61]. Here, it is also possible that an increase in high work hardening is due to load transfer occurring from the soft γ phase to the much stiffer α′ phase: the stiffer deformation-induced α′ phase is able to carry much higher loads when it forms in comparison to the parent γ phase [50,58]. Therefore, it is reasonable to observe lower work hardening in the 300 K test because of the lower levels of martensite transformed.

5 Conclusions

With neutron diffraction and TEM investigations, the following conclusions can be made regarding the formation of deformation-induced martensite in a 301 austenitic stainless steel. The first three conclusions are similar to work reported in the literature[22,48,49] for the 304 grade austenitic stainless steel. These conclusions are as follows:

1. Neutron diffraction results showed distinct transformation kinetics: one at 300 K and another at temperatures between 263 K and 100 K. At room temperature, transformation is slow and at 12% strain only 11% martensite was observed while at colder temperatures the same level of stress resulted in martensite fractions of 70-80%.
2. The rate and transformation sequence are different for the room and lower temperature experiments. At room temperature, the transformation sequence is $\gamma \rightarrow$ plastic deformation $\rightarrow \alpha'$, or $\gamma \rightarrow$ plastic deformation $\rightarrow \varepsilon$. For the lower temperature experiments, the transformation sequence is $\gamma \rightarrow \varepsilon \rightarrow \alpha'$.
3. The work hardening rate appears to have a direct relationship with the fraction of martensite formed.
4. The Schmid factor gives an indication of which grain families should, on average, plastically deform greater. At room temperature, this appears to indicate that grains more likely to plastically deform transform more readily. At 100 K no such preferential transformation is observed. This difference indicates that at room temperature, slip is more energetically favourable to accommodate strain energy than transformation, until sufficient nucleating sites are formed; whereas, at 100 K, due to the suppression of slip at lower temperatures, this is not the case.

Acknowledgements

The authors are grateful to the UK Science and Technology Facilities Council for the beam time granted at the ISIS facility (ENGIN-X beamline). MEF is grateful for funding from the Lloyd's Register Foundation, a charitable foundation helping to protect life and property by supporting engineering-related education, public engagement and the application of research. THS acknowledges support from the European Regional Development Fund via the Ser Cymru II fellowship program.

6 References

1. Ferreira, H. *et al.* Deformation Induced Martensite in an AISI 301LN Stainless Steel : Characterization and Influence on Pitting Corrosion Resistance. *Mater. Res.* **10,** 359–366 (2007).

2. Wong, S. L., Madivala, M., Prahl, U., Roters, F. & Raabe, D. A crystal plasticity model for twinning- and transformation-induced plasticity. *Acta Mater.* **118,** 140–151 (2016).

3. Frommeyer, G., Brüx, U. & Neumann, P. Supra-Ductile and High-Strength Manganese-TRIP/TWIP Steels for High Energy Absorption Purposes. *ISIJ Int.* **43,** 438–446 (2003).

4. Moat, R. J. *et al.* Work hardening induced by martensite during transformation-induced plasticity in plain carbon steel. *Acta Mater.* **60,** 6931–6939 (2012).

5. Olson, G. & Cohen, M. Stress-assisted isothermal martensitic transformation: application to TRIP steels. *Metall. Trans. A* **13,** 1907–1914 (1982).

6. Talonen, J. Effect Strain-Induced α'-Martensite Transformation on Mechanical Properties of Metastable Austenitic Stainless Steels. *Department of Mechanical Engineering* **PhD,** (Helsinki University of Technology, 2007).

7. Lecroisey, F. & Pineau, A. Martensitic transformations induced by plastic deformation in the Fe-Ni-Cr-C system. *Metall. Trans.* **3,** 391–400 (1972).

8. Zackay, V., Parker, E., Fahr, D. & Busch, R. The enhancement of ductility in high-strength steels. *ASM Trans Quart* (1967).

9. Tomita, Y. & Iwamoto, T. Constitutive modeling of TRIP steel and its application to the improvement of mechanical properties. *Int. J. Mech. Sci.* **37,** (1995).

10. Bain, E. C. & Dunkirk, N. Y. The nature of martensite. *trans. AIME* **70,** 25–47 (1924).

11. Frank, F. . Martensite. *Acta Metall.* **1,** 15–21 (1953).

12. Bolling, G. F. & Richman, R. H. The plastic deformation of ferromagnetic face-centred cubic Fe-Ni-C alloys. *Philos. Mag.* **19,** 247–264 (1969).

13. Angel, T. Formation of martensite in austenitic stainless steels. *J. Iron Steel Inst* **177,** 165–174 (1954).

14. Delogu, F. A few details of the austenite to martensite phase transformation in 304 stainless steel powders under mechanical processing. *Acta Mater.* **59,** 2069–2074 (2011).

15. Tsuchida, N., Yamaguchi, Y., Morimoto, Y., Tonan, T. & Takagi, Y. Effects of Temperature and Strain Rate on TRIP Effect in SUS301L Metastable Austenitic Stainless Steel. *ISIJ Int.* **53,** 1881–1887 (2013).

16. Tian, Y., Gorbatov, O. I., Borgenstam, A., Ruban, A. V. & Hedstr??m, P. Deformation Microstructure and Deformation-Induced Martensite in Austenitic Fe-Cr-Ni Alloys Depending on Stacking Fault Energy. *Metall. Mater. Trans. A Phys. Metall. Mater. Sci.* **48,** 1–7 (2016).

17. Das, Y. B. *et al.* In situ observation of strain and phase transformation in plastically deformed 301 austenitic stainless steel. *Mater. Des.* **112,** 107–116 (2016).

18. Tian, Y., Lienert, U., Borgenstam, A., Fischer, T. & Hedström, P. Martensite formation during incremental cooling of Fe-Cr-Ni alloys: An in-situ bulk X-ray study of the grain-averaged and single-grain behavior. *Scr. Mater.* **136,** 124–127 (2017).

19. Patel, J. R. & Cohen, M. Criterion for the action of applied stress in the martensitic transformation. *Acta Metall.* **1,** 531–538 (1953).

20. Wayman, C. M. & Bhadeshia, H. K. D. H. *Physical Metallurgy*. *Physical Metallurgy* **II,** (Elsevier, 1996).

21. Staudhammer, K. P., Murr, L. E. & Hecker, S. S. Nucleation and evolution of strain-induced martensitic (b.c.c.) embryos and substructure in stainless steel: A transmission electron microscope study. *Acta Metall.* **31,** 267–274 (1983).

22. Hecker, S. S., Stout, M. G., Staudhammer, K. P. & Smith, J. L. Effects of Strain State and Strain Rate on Deformation-Induced Transformation in 304 Stainless Steel : Part 1 . Microstructural Study. *Metall. Trans. A* **13,** 627–635 (1982).

23. Bhadeshia, H. Worked Examples in the Geometry of Crystals', 1987. *London, Inst. Met.*

24. Jimenez-Melero, E. *et al.* Martensitic transformation of individual grains in low-alloyed TRIP steels. *Scr. Mater.* **56,** 421–424 (2007).

25. Blondé, R. *et al.* High-energy X-ray diffraction study on the temperature-dependent mechanical stability of retained austenite in low-alloyed TRIP steels. *Acta Mater.* **60,** 565–577 (2012).

26. Jimenez-Melero, E. *et al.* The effect of aluminium and phosphorus on the stability of individual austenite grains in TRIP steels. *Acta Mater.* **57,** 533–543 (2009).

27. Jimenez-Melero, E. *et al.* Characterization of individual retained austenite grains and their stability in low-alloyed TRIP steels. *Acta Mater.* **55,** 6713–6723 (2007).

28. Blondé, R. *et al.* Mechanical stability of individual austenite grains in TRIP steel studied by synchrotron X-ray diffraction during tensile loading. *Mater. Sci. Eng. A* **618,** 280–287 (2014).

29. G. B. Olson & M. Cohen. A mechanism for the strain-induced martensitic transformations. *J. Less-Common Met.* **28,** 107–118 (1972).

30. Olson, G. & Cohen, M. Kinetics of strain-induced martensitic nucleation. *Metall. Trans. A* **6A,** 791–795 (1975).

31. Talonen, J. & Hänninen, H. Formation of shear bands and strain-induced martensite during plastic deformation of metastable austenitic stainless steels. *Acta Mater.* **55,** 6108–6118 (2007).

32. Hedström, P., Lienert, U., Almer, J. & Odén, M. Stepwise transformation behavior of the strain-induced martensitic transformation in a metastable stainless steel. *Scr. Mater.* **56,** 213–216 (2007).

33. Hedström, P. Deformation and Martensitic Phase Transformation in Stainless Steels. (2007).

34. Hedström, P., Han, T. S., Lienert, U., Almer, J. & Odén, M. Load partitioning between single bulk grains in a two-phase duplex stainless steel during tensile loading. *Acta Mater.* **58,** 734–744 (2010).

35. Lee, T. H., Shin, E., Oh, C. S., Ha, H. Y. & Kim, S. J. Correlation between stacking fault energy and deformation microstructure in high-interstitial-alloyed austenitic steels. *Acta Mater.* **58,** 3173–3186 (2010).

36. Lee, T. H. *et al.* An intersecting-shear model for strain-induced martensitic transformation. *Acta Mater.* **61,** 7399–7410 (2013).

37. Abreu, H. F. G. De, Silva, M. J. G. Da, Herculano, L. F. G. & Bhadeshia, H. Texture analysis of deformation induced martensite in an AISI 301L stainless steel: microtexture and macrotexture aspects. *Mater. Res.* **12,** 291–297 (2009).

38. Edwards, L., Fitzpatrick, M., Daymond, M. & Johnson, M. ENGIN-X: A neutron stress diffractometer for the 21st century. *Proc. 6th Intl. Conf.* (2000).

39. Santisteban, J. R., Daymond, M. R., James, J. A. & Edwards, L. ENGIN-X: A third-generation neutron strain scanner. *J. Appl. Crystallogr.* **39,** 812–825 (2006).

40. Kirichek, O. *et al.* Sample environment for neutron scattering measurements of internal stresses in engineering materials in the temperature range of 6 K to 300 K. *Rev. Sci. Instrum.* **88,** 025103 (2017).

41. ASTM. *ASTM E8 / E8M - 13a Standard Test Methods for Tension Testing of Metallic Materials*.

42. Fitzpatrick, M. E. & Lodini, A. *Analysis of Residual Stress by Diffraction using Neutron and Synchrotron Radiation*.

43. Oliver, E. ., Mori, T., Daymond, M. . & Withers, P. . Neutron diffraction study of stress-induced martensitic transformation and variant change in Fe–Pd. *Acta Mater.* **51,** 6453–6464 (2003).

44. Paddea, S. Stress and creep damage evolution in materials for ultra-supercritical power plants. **1,** (The Open University, 2013).

45. Harjo, S., Tsuchida, N., Abe, J. & Gong, W. Martensite phase stress and the strengthening mechanism in TRIP steel by neutron diffraction. *Sci. Rep.* **7,** 15149 (2017).

46. Hutchings, M. T., Withers.P.J, Holden, T. M. & Lorentzen, T. *Introduction to characterization of residual stress by neutron diffraction*. *Materials Today* **8,** (2005).

47. Astm. Standard Practice for X-Ray Determination of Retained Austenite in Steel with Near Random Crystallographic Orientation 1. *ASTM* **03,** 1–7 (2009).

48. De, A. K., Murdock, D. C., Mataya, M. C., Speer, J. G. & Matlock, D. K. Quantitative measurement of deformation-induced martensite in 304 stainless steel by X-ray diffraction. *Scr. Mater.* **50,** 1445–1449 (2004).

49. De, A. K. *et al.* Deformation-induced phase transformation and strain hardening in type 304 austenitic stainless steel. *Metall. Mater. Trans. A* **37,** 1875–1886 (2006).

50. Spencer, K., Embury, J. D., Conlon, K. T., Véron, M. & Bréchet, Y. Strengthening via the formation of strain-induced martensite in stainless steels. *Mater. Sci. Eng. A* **387–389,** 873–881 (2004).

51. Mangonon, P. L. & Thomas, G. The martensite phases in 304 stainless steel. *Metall. Trans.* **1,**

1577–1586 (1970).

52. Brooks, J. W., Loretto, M. H. & Smallman, R. E. In situ observations of the formation of martensite in stainless steel. *Acta Metall.* **27,** 1829–1838 (1979).

53. Brooks, J. W., Loretto, M. H. & Smallman, R. E. Direct observations of Martenstte Nuclei in Stainless steel. *Acta Metall.* **27,** 1839–1847 (1979).

54. Yang, X. S., Sun, S., Wu, X. L., Ma, E. & Zhang, T. Y. Dissecting the mechanism of martensitic transformation via atomic-scale observations. *Sci. Rep.* **4,** 1–7 (2014).

55. Gey, N., Petit, B. & Humbert, M. Electron backscattered diffraction study of ε/α′ martensitic variants induced by plastic deformation in 304 stainless steel. *Metall. Mater. Trans. A* **36,** (2005).

56. Das, Y. B. *et al.* An experimental study of plastic deformation and transformation in austenitic stainless steel. *Unpubl. Work*

57. Bachmann, F., Hielscher, R. & Schaeben, H. Grain detection from 2d and 3d EBSD data-Specification of the MTEX algorithm. *Ultramicroscopy* **111,** 1720–1733 (2011).

58. Hedström, P. *et al.* Load partitioning and strain-induced martensite formation during tensile loading of a metastable austenitic stainless steel. *Metall. Mater. Trans. A Phys. Metall. Mater. Sci.* **40,** 1039–1048 (2009).

59. Nagy, E., Mertinger, V., Tranta, F. & Sólyom, J. Deformation induced martensitic transformation in stainless steels. *Mater. Sci. Eng. A* **378,** 308–313 (2004).

60. Choi, J.-Y. & Jin, W. Strain induced martensite formation and its effect on strain hardening behavior in the cold drawn 304 austenitic stainless steels. *Scr. Mater.* **36,** 99–104 (1997).

61. Ennis, B. L. *et al.* Metastable austenite driven work-hardening behaviour in a TRIP-assisted dual phase steel. *Int. J. Plast.* **88,** 126–139 (2017).